ADVANCED MATERIALS INTERFACES
Open Access
www.advmatinterfaces.de

Inhomogeneity of Cleaved Bulk MoS_2 and Compensation of Its Charge Imbalances by Room-Temperature Hydrogen Treatment

Erika Giangrisostomi, Ruslan Ovsyannikov, Robert Haverkamp, Nomi L. A. N. Sorgenfrei, Stefan Neppl, Hikmet Sezen, Fredrik O. L. Johansson, Svante Svensson, and Alexander Föhlisch*

Synthetic single crystals of bulk molybdenum disulphide cleaved in ultrahigh vacuum are mapped across a large (≈25 mm^2) area by X-ray photoelectron spectroscopy, both statically and transiently following above-bandgap excitation by an ultrafast laser. This work finds that: I) A cleaved surface typically displays spatially inhomogeneous properties, manifested by large (≈1 eV) variations in binding energy and band bending and variable degrees of stability of those over time as a result of variable gas uptakes from the residual atmosphere. II) Moderate (350 °C) annealing and exposure to molecular hydrogen can be cycled to switch between smaller and larger surface band bending, the switch being reversible but strongly sample-position dependent. III) Upon exposure to atomic hydrogen, the binding energy of the entire surface levels out to a common (within <0.05 eV) value corresponding to a Fermi level pinned close to mid-bandgap. Such remarkable effect is attributed to the ability of hydrogen atoms to serve as donors and acceptors alike, thus neutralizing local charge imbalances inevitably present at the surface in consequence of intrinsic and/or cleavage-induced defects. With subsequent moderate annealing, the hydrogenated surface preserves a fairly homogenous electronic state which is however characterized by a lower binding energy and little to no band bending.

1. Introduction

Molybdenum disulphide (MoS_2) is a layered transition metal dichalcogenide with diverse and largely tuneable properties for plenty of applications—in electronics, photonics, chemo- and biosensing, energy storage, and catalysis.[1,2] While studies on mono- and few-layer MoS_2 have proliferated in recent years following a great surge of interest for 2D materials, bulk MoS_2 has remained relatively underexplored.

Previous investigations have raised the issue of the inhomogeneity and irreproducibility of the electronic properties of cleaved MoS_2(0001) surfaces. Large and continuous core-level binding energy (BE) variations across the surface have been reported by Mahatha et al.,[3] and tentatively ascribed to charged dislocations arising from the cleavage. In an earlier work, Mattila et al.[4] had

E. Giangrisostomi, R. Ovsyannikov, R. Haverkamp, N. L. A. N. Sorgenfrei, H. Sezen[++], F. O. L. Johansson[+++], A. Föhlisch
Institute Methods and Instrumentation for Synchrotron Radiation Research
Helmholtz-Zentrum Berlin
Albert-Einstein-Straße 15, 12489 Berlin, Germany
E-mail: erika.giangrisostomi@helmholtz-berlin.de; erika.giangri@gmail.com

The ORCID identification number(s) for the author(s) of this article can be found under https://doi.org/10.1002/admi.202300392

[+]Present address: Paul Scherrer Institute, Villigen Switzerland

[++]Present address: Technical University of Darmstadt, Germany

[+++]Present address: Sorbonne Université, Paris, France and Royal Institute of Technology, Stockholm Sweden

R. Haverkamp, N. L. A. N. Sorgenfrei, S. Neppl[+], F. O. L. Johansson[+++], A. Föhlisch
Institute of Physics and Astronomy
University of Potsdam
Karl-Liebknecht-Straße 24/25, 14476 Potsdam-Golm, Germany

S. Svensson
Division of X-ray Photon Science
Department of Physics and Astronomy
Uppsala University
P.O. Box 516, Uppsala 751 20, Sweden

DOI: 10.1002/admi.202300392

proposed a similar explanation based on cleavage-induced steps for the low BE minority components in their S 2p X-ray photoelectron spectroscopy (XPS) spectra. N- and p-type semiconducting behaviors have both been observed at different locations on the same sample by McDonnell et al.[5] The latter study has also pointed to a correlation between current-voltage characteristics, core-level BE variations, and changes in sample stoichiometry (from XPS) and surface defect density (from scanning tunneling microscopy), whereby p-type behavior has been associated with lower S 2p BEs, an excess concentration of sulfur atoms and a higher density of surface defects. In contrast, Donarelli et al.[6] and Zhang et al.[7] have interpreted the low BE minority component in their S 2p XPS spectra as due to the presence of sulfur vacancies. The former authors[6] have also shown continuously decreasing core-level BEs with increasing annealing temperatures until 400 °C, which was attributed to Fermi level pinning to states induced in the bandgap by an increasing concentration of sulfur vacancies. This attribution contradicts earlier statements by Lince et al.[8] that annealing up to 1000 °C removes contaminants without forming defects, or by Papageorgopoulos et al.[9] that, vice versa, the shift to lower core-level BEs with short annealing at 1000 °C is caused by a loss of donor states from the bandgap as the sample turns into a more intrinsic semiconductor.

In consideration of these findings, even when the MoS_2 bulk single crystal should start out of excellent quality, it appears challenging to obtain from it a clean surface without compromising its native properties. This has a ripple effect when trying to establish the properties of MoS_2 in relation to extrinsic dopants, metal contacts or within heterostructures with other semiconductors. While an ideal MoS_2(0001) surface is expected to be chemically inert and only subject to small charge transfer from physisorbed or intercalated molecules, the presence of defects is likely to foster stronger interactions, which in some cases can lead to dissociative adsorption. Such mechanisms are key in gas sensing applications[10] and represent the basis for the success of MoS_2 as a catalyst.[11] Several first-principles calculation studies on the interaction of monolayer MoS_2 with environmental gas molecules (N_2, O_2, CO_2) and gas molecules that are likely to be prevalent in the residual atmosphere of an ultrahigh vacuum (UHV) chamber (H_2O, H_2, CO) predicted that these mostly act as charge acceptors.[12,13] Experimental studies looking at their effects on monolayer MoS_2-based devices have accordingly shown that ambient conditions mostly induce p-type doping in otherwise n-type monolayer samples, which is detrimental for field effect transistors[14] but beneficial for light emitters.[15] However, surprisingly few studies have directly addressed the interaction of those common molecules with bulk MoS_2, and arguably none with a systematic approach allowing to relate it to the properties of the likely heterogeneous starting conditions of its surface.

When it comes, in particular, to the interaction of MoS_2 with hydrogen—which is crucial for understanding the hydrodesulfurization (HDS)[16] and hydrogen evolution (HER)[17] catalytic reactions, as well as the hydrogen storage capacity of MoS_2[2]—calculations for small monolayer clusters depict the following scenario. H_2 molecules are predicted to dissociatively adsorb at sulfur vacancies, be they defects on the basal plane[13] or the uncoordinated sites of the edge surface.[18] Moreover, it is known from the context of HDS catalysis that, at very high pressures and favored by high temperatures, H_2 molecules dissociatively adsorb and then leave the surface as H_2S, thereby generating sulfur vacancies.[19] Otherwise H_2 molecules are expected to be only weakly physisorbed at the surface. Previous studies[12,20,21] report different but relatively small negative adsorption energies. The energy barrier for H_2 diffusion from one side to the other of one MoS_2 layer is calculated by Koh et al.[22] as ≈6.56 eV, but estimated to be greatly suppressed by both sulfur vacancies and strain. Inserting a H_2 molecule between two MoS_2 layers is calculated by Zhu et al.[23] to require an energy of ≈0.53 eV, and estimated to lead to only minor interlayer expansion. H_2 physisorbed in the interlayer space is anticipated to leave the electronic structure substantially unaffected.[24,21] The situation is very different for atomic hydrogen. Calculations of the adsorption energies as a function of the Fermi level position for the three charge states and various adsorption geometries are provided by Cai et al.[25] Calculations of the formation energies of H interstitials as a function of the Fermi level position for the three charge states can be found in Zhu et al.[23] Calculations of adsorption energies as well as substitution energies as a function of H concentration are given by Xu et al.[26] The picture which emerges from Cai et al.[25] is that H is most easily adsorbed in its positively charged state on monolayer MoS_2, thus leading to n-type doping and that, with increasing H uptake, H-induced defect levels in the MoS_2 bandgap evolve into delocalized bands which confer one-dimensional metallic character and cause Jahn–Teller distortion of the lattice. Xu et al.[26] draw a similar picture, indicating 12.5% as the concentration of H beyond which 1H-MoS_2 becomes metallic. According to Yakovkin et al.,[24] H intercalation between two MoS_2 layers induces an in-plane shift such that the S atoms on the two planes align on top of each other, such system being metallic and characterized by a 5-fold increase in binding energy between the layers due to forming S-H-S bonds.

From an experimental point of view, there are relatively few works concerned with the interaction between bare MoS_2 and hydrogen outside of the electrocatalytic context. For monolayer MoS_2 grown by chemical vapor deposition (CVD) and wet transferred onto a hydrogenated-graphene/SiC substrate, Pierucci et al.[27] actually obtained a seemingly opposite result: cumulative exposure to atomic H at room temperature was reported to lead to increased p-type doping, based on a BE decrease in XPS. They explained their finding in terms of H atoms passivating S vacancies, S vacancies being believed as the source of the original n-type doping. Results along the line of the aforementioned theoretical predictions for monolayer MoS_2 interacting with H were instead obtained for single-crystal MoS_2 flakes exposed to H_2 at 300 °C by Han et al.[28] After cleaved MoS_2 was exposed to H_2 at 300 °C, transmission electron microscopy revealed areas of the original 2H phase, areas with desorbed S atoms, and areas where the upper S plane had glided with respect to the bottom S plane of the same top layer somewhat half-way between the 2H and 1T phases, overall leading to a huge conductivity increase. In a subsequent study by the same first author,[29] bulk MoS_2 samples were investigated with XPS applying different combinations of cleaving, annealing and H_2 exposure. The featured result is that, upon H_2 exposure, all XPS signals are subject to a drastic intensity reduction and the S 2p spectrum sees the appearance of a new component at about 1 eV higher BE than the main peak, which is read as a signature of H_2 dissociative adsorption at sulfur vacancies. However, the same work also hints at different

behaviors from sample positions characterized by different initial S 2p BEs, spanning from no effect of H_2 exposure nor of subsequent annealing, to no effect of H_2 exposure but large shift to lower BE and growth of a tail on the high BE side of the main peak upon subsequent annealing, to significant shift to higher BE of the entire S 2p spectrum upon H_2 exposure.

Here we present an XPS investigation of bulk 2H-phase MoS_2 single crystals commercially grown by chemical vapor transport, that aims to shed light on the unsettled aspects described above: inhomogeneity of the cleaved surface, effect of moderate vacuum annealing, response to gases from the residual atmosphere of the vacuum chamber, and response to controlled room temperature exposure to both molecular and atomic hydrogen. By mapping millimeter-sized samples with surface-sensitive XPS, we provide clear evidence for the electronic inhomogeneities characterizing a cleaved surface of bulk MoS_2. We show that vacuum annealing at 350 °C usually results in a surface free of contaminants, yet still characterized by a variety of BE and band bending characteristics, which drive different propensities and dynamic responses to gas uptake. Finally, we demonstrate that such inhomogeneity of the surface electronic structure can be largely lifted by exposure to atomic hydrogen. We therefore suggest that atomic hydrogen is a simple but effective agent to neutralize charged defects at the MoS_2 surface.

2. Results and Discussion

We will illustrate our findings mainly through the results obtained from what we will refer to as sample 1, for which the most extensive dataset was acquired. Additional results from a different sample, referred to as sample 2, will be hinted at in the main text and presented in Supporting Information to underscore the generality of the main findings and describe complementary aspects.

Both samples were cleaved by scotch tape a first time in air shortly before transfer into the UHV system, then a second time under UHV conditions shortly before the start of the XPS measurements. The measurement setup, at the LowDosePES end-station[30] of the BESSY II synchrotron, is schematized in **Figure 1**c, right—with more details provided in the Experimental Section. The X-ray photon energies were chosen to yield photoelectrons at kinetic energies around 50 eV, thereby providing a probing depth which roughly encompasses the two topmost MoS_2 layers. Static XPS measurements have been complemented by time-resolved pump-probe XPS measurements following excitation by a green (photon energy of 2.4 eV, well above the 1.23-1.29 eV[31,32] bandgap of bulk MoS_2), ultrafast (pulse duration of ≈330 fs) pump laser beam, spatially overlapped and temporally synchronized to the probe X-ray beam. When the laser is OFF, the measured photoelectrons are representative of the energy levels of the very surface. With the laser-ON at a sufficiently high power, the photogenerated free carriers are able to screen a possible built-in electric field at the surface, in which case the photoelectrons can be assumed to carry information about the energy levels of the bulk.[33] Therefore, the combination of laser-OFF and laser-ON measurements provides experimental access to the surface band bending (Figure 1c, left).

Sample 1 was characterized according to the following procedure: S 2p spectra with laser-OFF and laser-ON and valence band spectra[34] were measured at a few positions soon after sample preparation ("pre-characterization"); the evolution of the S 2p spectra at these same positions was continuously monitored for several hours ("time traces"); S 2p spectra were collected across the entire sample surface—raster scanned at steps of 100 μm, which roughly equals the focal spot size of the X-ray beam ("XY maps"); for the positions emerged from these maps as most representative of the variability of the sample, S 2p spectra with laser-OFF and laser-ON were measured—including laser power series and pump-probe delay scans to confirm saturation conditions for the excitation—as well as valence band spectra and C 1s spectra ("post-characterization"). This same procedure was applied after each new treatment of the sample. The treatments for sample 1 were as listed in Figure 1b—namely, in chronological order: i) UHV cleaving, ii) annealing for 5 h at 350 °C, iii) annealing for 2 h at 350 °C, iv) annealing for 3 h at 350 °C followed by cooling down to room temperature (RT) and dosing of H_2 at 1×10^{-4} mbar pressure for 30 min, v) annealing for 3 h at 350 °C followed by cooling down to RT and dosing of H_2 at 1×10^{-4} mbar pressure for 30 min while heating a (pre-degassed) tungsten filament placed between the sample and the H_2 nozzle to promote the splitting of molecular hydrogen (H_2) into atomic hydrogen (H), vi) annealing for 3 h at 350 °C, vii) annealing for 3 h at 350 °C, viii) annealing for 2 h at 450 °C, ix) annealing for 3 h at 350 °C followed by cooling down to RT and dosing of H_2 at 1×10^{-4} mbar pressure for 30 min with cracking filament ON, x) annealing for 2 h at 350 °C, xi) exposure to ambient conditions for 1 h (plus venting and pumping times). For the preparations involving gas dosing (iv, v and ix), S 2p spectra with laser-OFF and laser-ON were additionally measured for the chosen representative positions also right after the pre-dosing annealing to assess the extent of reversibility of the previous preparation. For the intermediate annealing after the first H-dosing (preparation vii) and for the second H-dosing (preparation ix), only the precharacterization was performed, due to time constraints. From preparation iii) onwards, the positions for the pre-characterization and post-characterization were kept the same. The approximate locations of the latter are marked in Figure 1a on top of an image of the sample surface obtained from an ex situ optical microscope. Among them, one position—P3—was kept the same through the complete sequence of preparations.

The main results for the preparations i), ii), iv), v), and vi) are shown in **Figures 2–6**, respectively, where panels (a) are S 2p spectra from the pre-characterization (with laser-OFF in black and with laser-ON at +250 ps/+4 μs pump-probe delay and ≈30 μJ cm^{-2} pump energy density in red/blue), panels (b) and (c) are the fitted S $2p_{3/2}$ BE and full width at half maximum (FWHM) from the time traces, and panels (d) and (e) are the fitted S $2p_{3/2}$ BE and FWHM from the XY maps. For these preparations, **Figure 7** presents concisely the central findings relative to position P3, namely laser-OFF and laser-ON S 2p spectra (panel (a), left, solid and dotted lines, respectively) and valence band spectra (panel (a), right), plus a comparison of the angular-resolved photoelectron spectra (ARPES, panel (c)) and of the derived energy band diagrams (panel (b)) between the annealed and the H-dosed sample. The Supporting Information offers a different representation for these main results, plus it provides additional data relative to the other preparations of the same sample, and additional data relative

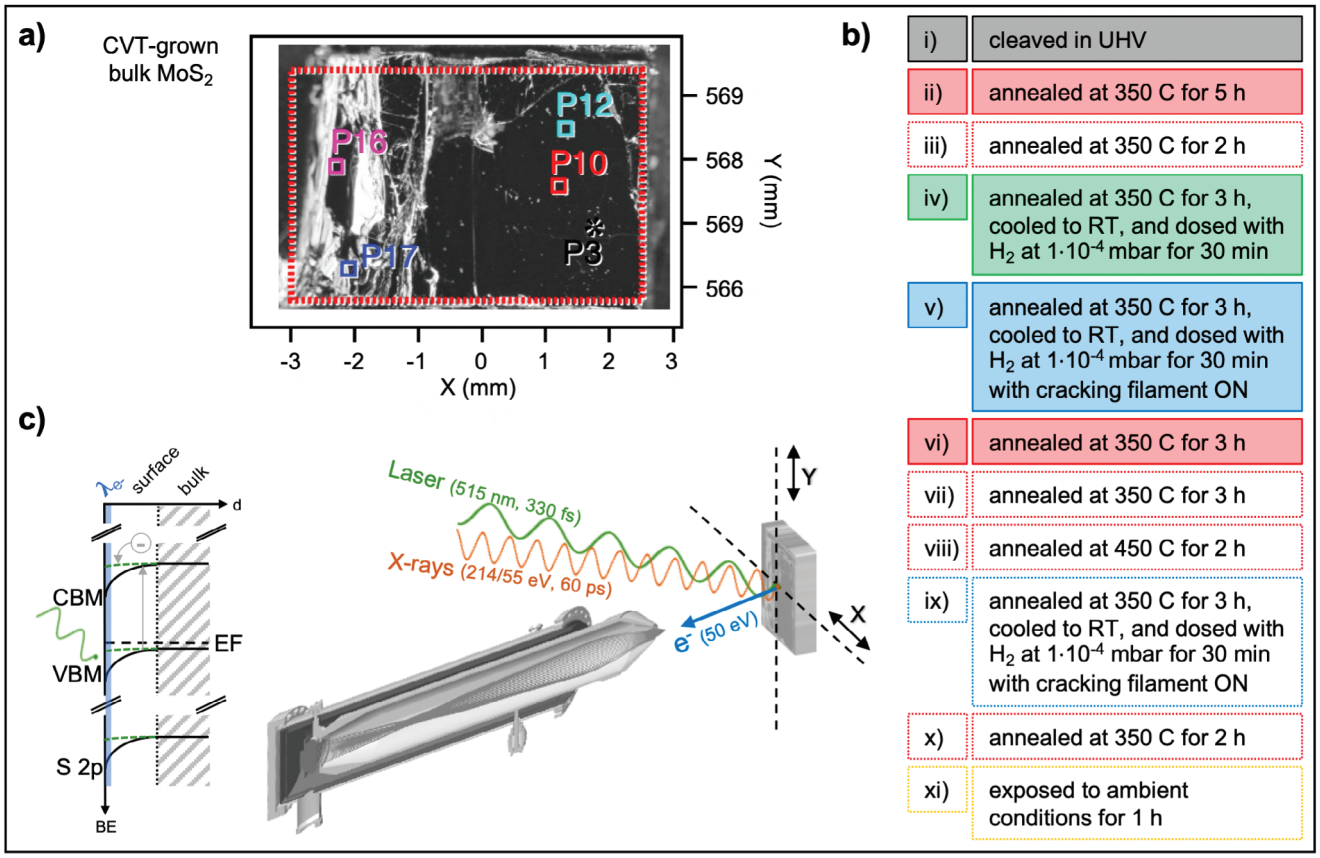

Figure 1. a) View of the studied CVT-grown bulk MoS_2 sample. Photograph showing the leftover material on the cleaving tape (left) and image from an optical microscope (right). Colored symbols on the latter mark the approximate location of the most extensively characterized positions. b) History of sample treatments. Colored backgrounds denote treatments whose results are presented in the main text, whereas the results of the other treatments are presented in the Supporting Information. c) Schematic representation of the experimental setup (right) and of the accessible spectroscopic variables (left). X-ray and laser beams, represented by orange and green arrows, respectively, are overlapped in both time and space on the sample surface, where they impinge at a 45° horizontal angle from the sample surface normal with a slight vertical offset to each other. The laser photons have an energy of 2.4 eV. The X-ray photons energy is varied such that photoelectrons from the S 2p core level and from the valence band are emitted with a kinetic energy of about 50 eV, which maximizes their surface sensitivity. Those photoelectrons, represented by a blue arrow, are collected by an angular-resolved time-of-flight (ArTOF) spectrometer at normal emission geometry. When the laser is OFF, photoelectrons are representative of the energy levels of the very surface. When the laser is ON at a sufficiently high power, the photogenerated free carriers can fully compensate for the possible built-in electric field near the surface due to band bending, and therefore carry information about bulk-like energy levels. The position of the conduction band minimum (CBM) is estimated from the measured position of the valence band maximum (VBM) and a nominal bandgap of 1.3 eV.

to a similar sequence of preparations of a second sample. In particular, Figures S3–S5 (Supporting Information) each focus on one of three selected positions for sample 1 following the evolution of their S 2p and valence band spectra across all sample treatments.

2.1. Cleaving and Annealing

The sample surface presents a high degree of inhomogeneity after cleavage. Based on the measurements of Figure 2a, looking at the location of the measured positions in Figure 2d,e and comparing them with the images in Figure 1a (including the photo showing the profile of the leftover material on the cleaving tape), it seems that the well-cleaved, flatter regions on the right side of the sample (P1, P2, P3) exhibit lower BEs, smaller laser-induced shifts toward higher BEs, smaller FWHM and higher intensities with respect to the poorly-cleaved,[35] more corrugated regions on the left side of the sample (P4, P5, P6). The valence band spectra mirror the BE variations of the core level spectra, with an offset of 161.4 ± 0.25 eV between the positions of the S $2p_{3/2}$ peak and of the valence band maximum (VBM) at the Γ point being a constant throughout all sample positions and preparations. The only identifiable contaminant is carbon. To our experience, the latter is always present if the sample is uncleaved and most often absent if the sample cleaved properly. This is the case for sample 2. However here, for sample 1, also well-cleaved positions exhibit some carbon contamination. As already pointed out by Kadowaki et al.,[36] this suggests that the bulk crystal can include contaminated interfaces, in which case cleaving would be likely to preferentially occur at such interfaces.

As visible in Figure 2b, uncleaved positions maintain their high BEs over time, whereas well-cleaved positions are subject to an increase in their BEs, which continues for several hours

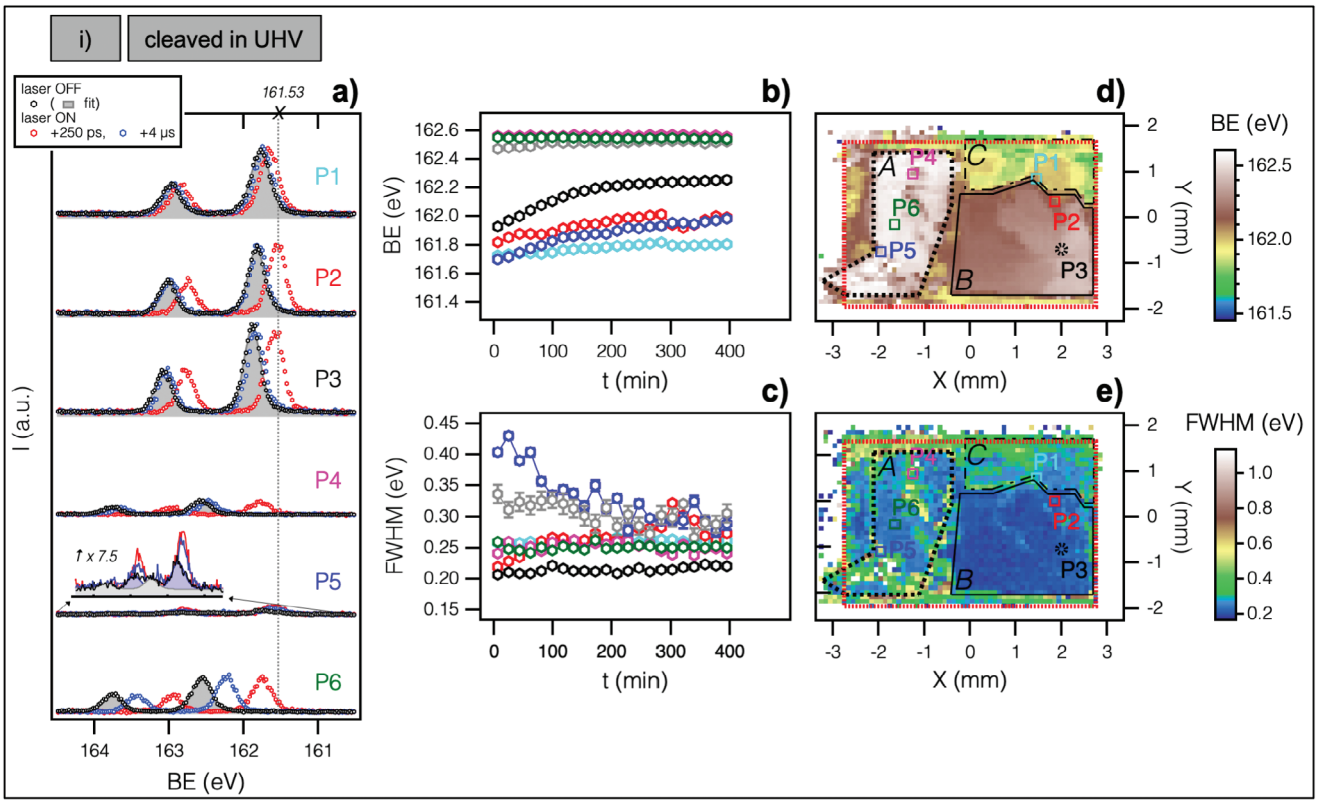

Figure 2. Treatment step (i): sample cleaved in ultrahigh vacuum (UHV). a) S 2p laser-OFF (black, fit in gray) and laser-ON (red/blue at +250 ps/+4 µs pump-probe delays and ≈30 µJ cm^{-2} pump energy density) X-ray photoelectron spectroscopy (XPS) spectra for selected positions (P#), recorded immediately after sample preparation. b,c) Evolution of the fitted (laser-OFF) S 2$p_{3/2}$ binding energy (BE)/full width at half maximum (FWHM) for the same selected positions (see color code) as a function of time. For P5 two doublets are present (fit results in blue and gray). d,e) Map of the fitted (laser-OFF) S 2$p_{3/2}$ BE/FWHM as a function of sample lateral coordinates, recorded several hours after sample preparation at the stabilization of the changes shown in (b,c), also referred to as "XY maps". The location of the selected positions is marked, as well as the approximate perimeter of three distinctively different regions (A, B, C, delimited by black lines). The red rectangle encloses the area over which (laser-OFF) S 2$p_{3/2}$ BE and FWHM histograms for this preparation are calculated (see Figure S2, Supporting Information).

before eventually saturating. No correlation is apparent between the initial BE value and the rate and magnitude of the BE increase over time, nor between those quantities and the trend followed by the FWHM, which can be seen in Figure 2c to stay constant as well as to increase or decrease with time (see also Figure S8, Supporting Information, for more data from sample 2). All time traces were obtained by cycling the probed spot among the chosen positions, hence the horizontal axis represents a common timescale. Also, since the measurements were started within few minutes after UHV cleavage, such shared time axis represents both the time elapsed since UHV cleavage and the time spent under the X-ray beam. However, in consideration of additional data from sample 2–reported in Figure S8 (Supporting Information)—where the acquisition for certain positions was delayed with respect to the introduction of the sample in the main chamber and where some other positions were exposed less frequently to the X-rays, we judge that the observed temporal changes reflect the interaction of the sample with the residual gases in the measurement chamber, rather than possible X-ray-induced effects. The latter are indeed expected to be minimal, given the low flux characteristics of the chosen X-ray beamline.[30]

While a large variability in the surface electronic structure was expected based on the works mentioned earlier, we are not aware of any other author having reported about drifts in XPS spectra taking place during measurements in UHV. Addou et al.[37] observed what could be the counterpart of our BE increase over time, namely a decrease in work function for geological bulk MoS_2 crystals with time after exfoliation, a decrease that different samples displayed with variable amounts and variable time constants, and which they attributed to adsorption of contaminants. A substantial difference is, however, that such changes were observed in Kelvin probe measurements carried out in air. Other authors[38,39] who have investigated few-layer and monolayer films grown by CVD have, on the contrary, observed an increase in work function with ambient contamination, interpreted as hole-doping in accord with the aforementioned studies.[12–15] It is therefore apparent that the doping behavior of bulk samples is distinctly different from the much more studied doping behavior of thin films, which have a different electronic structure, are subject to different dielectric effects and are affected by interactions with the substrate.[40–42]

The XY maps collected after the temporal drifts in BE had reached saturation at the monitored positions allow to relate

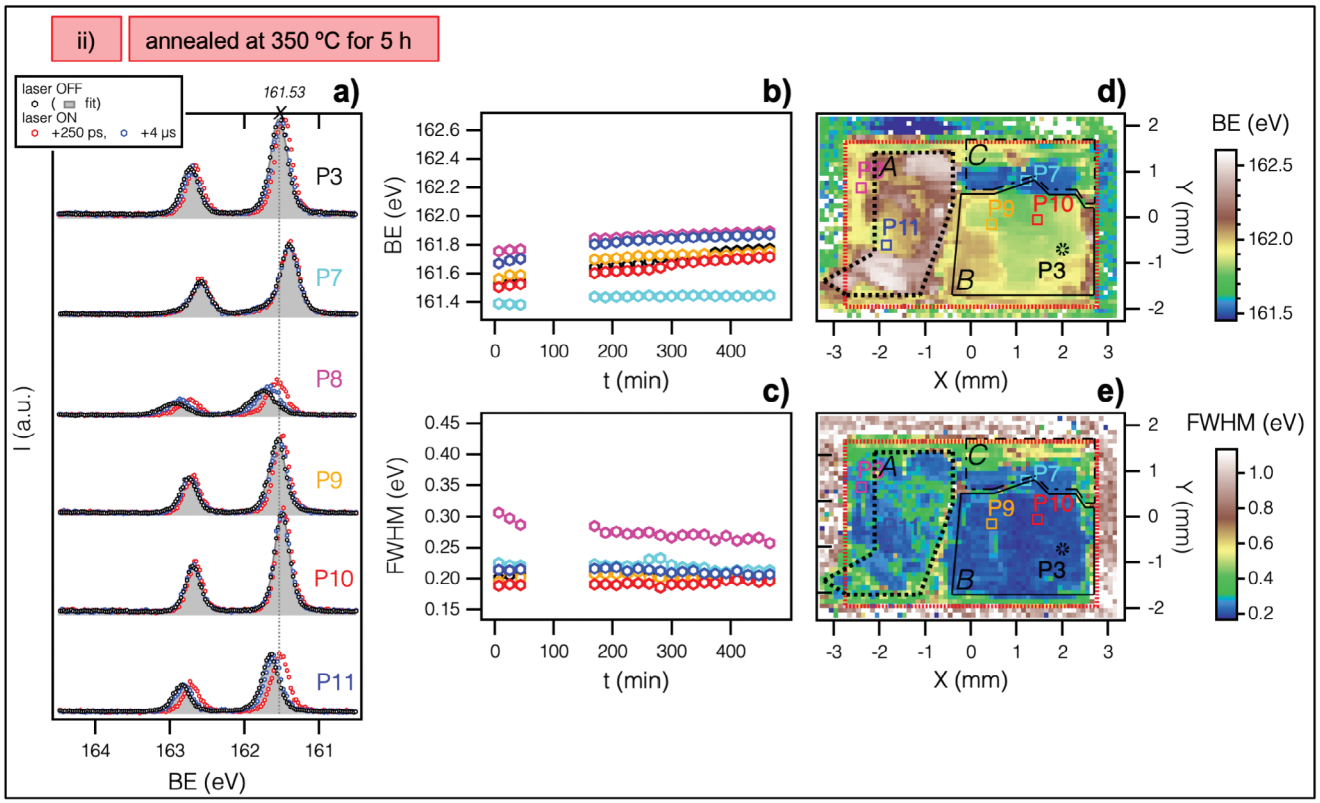

Figure 3. Treatment step (ii): sample annealed (in ultra-high-vacuum (UHV)) at 350 °C for 5 h. Same plots as described in the caption of Figure 2. Note that the selected positions are different, except for P3. The value of 161.53 eV for the S $2p_{3/2}$ binding energy (BE) of P3 at this preparation (vertical dotted line in panel (a)) is chosen as a reference against which all positions at all preparations can be readily compared.

specific spectral features and their behaviors upon subsequent sample treatments to the location of the respective spot within a specific macroscopic region. This endows with statistical robustness inferences that may otherwise be considered just anecdotal when measuring only few spots or even incorrect when not paying explicit attention to the selection of the probed spot and its reproducibility across the various measurements. According to Figure 2d,e, three chiefly different areas can be identified for sample 1: the left half—region A, marked with a dotted line—which is an uncleaved area characterized by the highest BEs and relatively large FWHM, the right bottom portion—region B, marked with a solid line—which is a well-cleaved area characterized by intermediate BEs and the smallest FWHM, and the smaller portion on the right top—region C, marked with a dashed line—which is also a well-cleaved area but characterized by the lowest BEs and relatively large FWHM. The largest FWHM is found at the borders between these regions and in stripes within region A, and correspond—understandably—to the most corrugated parts of the surface. The surface corrugation was roughly assessed during the experiment through a microscope camera available at the analysis chamber (with respect to whose field of view the position of the X-ray focus was known). A more precise quantification was possible a posteriori based on the XY maps themselves, since each spectrum—having been acquired through an angular-resolved time-of-flight spectrometer—can be analyzed to bring information on the misalignment of the corresponding sample position relative to an ideally flat surface placed at the proper working distance to the spectrometer. Examples of such XY maps of the relative sample height are provided in Figure S12 (Supporting Information) for as-cleaved sample 1 and sample 2 (left and right panels, respectively), together with the XY maps of the respective S 2p BEs.

Figure 3 shows the results of the next treatment step: annealing at 350 °C for 5 h. This first annealing cycle is effective in removing C, which will no longer be detected at any probed positions on sample 1 henceforth. At the same time, all laser-OFF spectra shift to lower BEs—in line with previous observations[6,9]—so that the laser-induced BE shifts become apparently small at the uncleaved positions (Figure 3a, P8, P11) and null at the cleaved positions (Figure 3a, P3, P7, P9, P10). Over time, all positions are still susceptible to drifts toward higher BEs, yet the asymptotic BE values are not as high (Figure 3b versus Figure 2b). Indeed, the overall BE distribution is peaked at lower values than in the corresponding map before annealing (Figure 3d versus Figure 2d, and Figure S2, Supporting Information). BEs and FWHM get more scattered within the identified regions, with portions at the middle of region A becoming more similar to region B, region B acquiring portions of larger FWHM at the border with region A, and region C developing slightly redefined and sharper boundaries. Despite the great dynamicity displayed by the sample upon this first round of annealing, the XY maps of Figure 3d,e appear to reflect a well-equilibrated stable situation, given that a second round of annealing at the same temperature (treatment step (iii)) reproduces the results of the

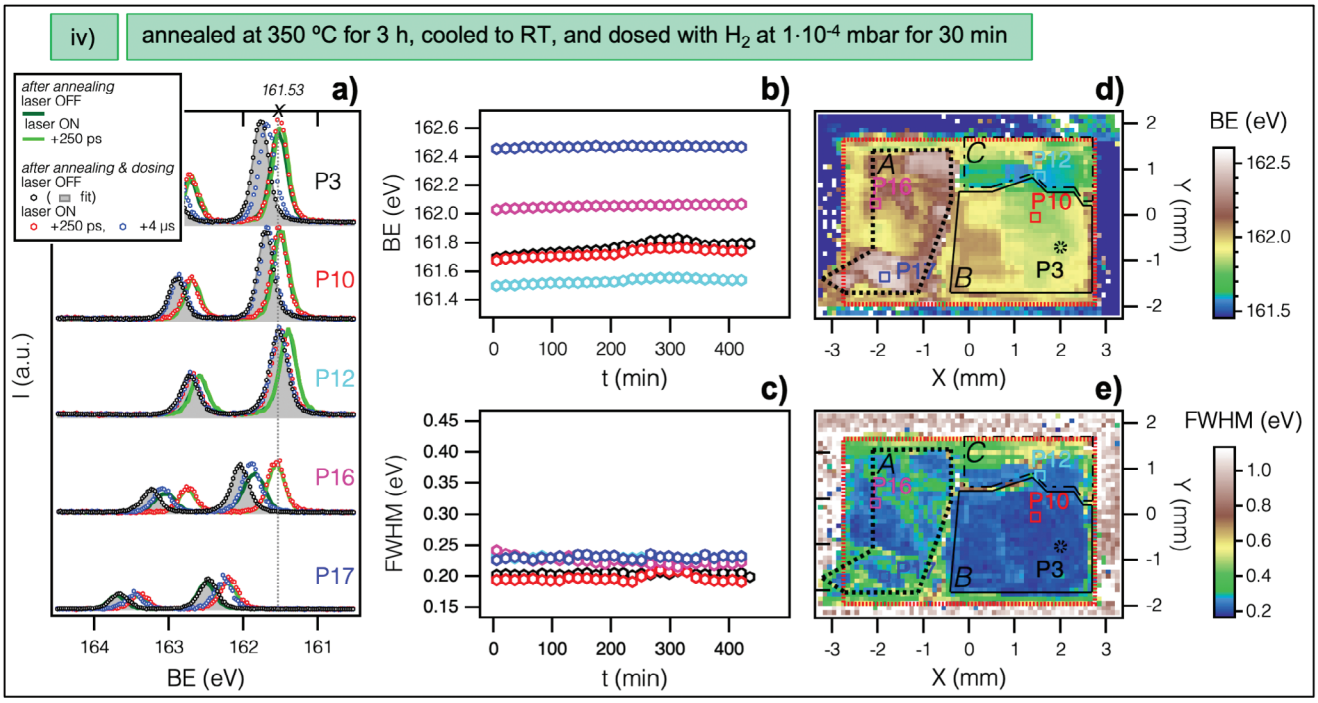

Figure 4. Treatment step (iv): sample annealed (in ultra-high-vacuum (UHV)) at 350 °C for 3 h, then cooled to room temperature, and finally dosed with H_2 at 1×10^{-4} mbar for 30 min. Same plots as described in the caption of Figure 2. Additionally, panel (a) shows S 2p laser-OFF (dark green) and laser-ON (light green, at +250 ps pump-probe delay and ≈30 µJ cm^{-2} pump energy density) X-ray photoelectron spectroscopy (XPS) spectra for the sample just cooled after annealing and right before gas exposure.

first round of annealing extremely well, both right after preparation and at the equilibration of changes many hours later, as it can be appreciated from the comparison of panels (a) and (d) in Figure S1 (Supporting Information). From this fact and from the fact that for region B the laser-ON spectra are unchanged, and the laser-OFF spectra are now coinciding with them, one may deduce that annealing at 350 °C has removed ambient contaminants from the surface without creating additional defects. The corresponding valence band spectra can then be taken as revealing of the doping of the bulk material. As shown in Figure 7 for position P3, the VBM is located ≈0.13 eV below the Fermi level,[43] which—considering a nominal bandgap of 1.23-1.29 eV[31,32]—qualifies our sample as heavily p-doped. Position P7 from region C stands out in that its BE is stable over time and its VBM coincides with the Fermi level. As for positions P8 and P11, they are unfortunately no longer representative of the highest BEs in region A; however, one can look at positions P16 and P17 from the preannealing stage of the next preparation step (Figure 4a), dark green and light green lines for laser-OFF and laser-ON measurements, respectively) and note that here the band bending remains large. Also, one can note that the laser-ON spectrum at P17 is not in trend with the others, but it is peaked at a significantly higher BE. We deduce from these observations that doping and adsorbates are not the only determinants of the measured energy levels, the latter being also impacted by disruptions in the sample topography. One further consideration is that a broad S 2p signal is appearing on the XY maps after annealing at the perimeter of the mapped area coming, not from the sample (the sample area is approximately enclosed within the red rectangles), but from the portion of the sample holder surrounding the sample, indication that a temperature of 350 °C is sufficient to promote desorption of sulfur atoms. At the same time, we do not detect—within the experimental uncertainty[44]—any notable decrease in the S 2p signal intensity from the sample. We therefore infer that sulfur atoms desorbed from the near-surface region are dynamically replaced by diffusion from the bulk. This is in agreement with the finding from Donarelli et al.[6] that annealing until at least 400 °C does not affect the surface stoichiometry of mechanically exfoliated MoS_2 (while it does for chemically exfoliated MoS_2 according to the same study).

2.2. Molecular and Atomic Hydrogen Exposure

From treatment step (iii) onwards, the monitored positions will remain the same. They are P3 and P10 belonging to region B, P12 belonging to region C and P16 and P17 belonging to region A.

The results of molecular hydrogen exposure are reported in Figure 4. H_2 exposure leaves only the highest BE position (P17) unaffected, while for all the other positions it leads to a BE increase of variable amount (Figure 4a). The laser-ON spectra remain unchanged for the other position in region A and for the positions in region B, which therefore see an increase in their laser-induced BE shifts. Instead, the laser-ON spectrum shifts by the same amount as the laser-OFF spectrum for the position belonging to region C (P12), which then retains its null laser-induced BE shift—possibly indicating that absorbed molecules can

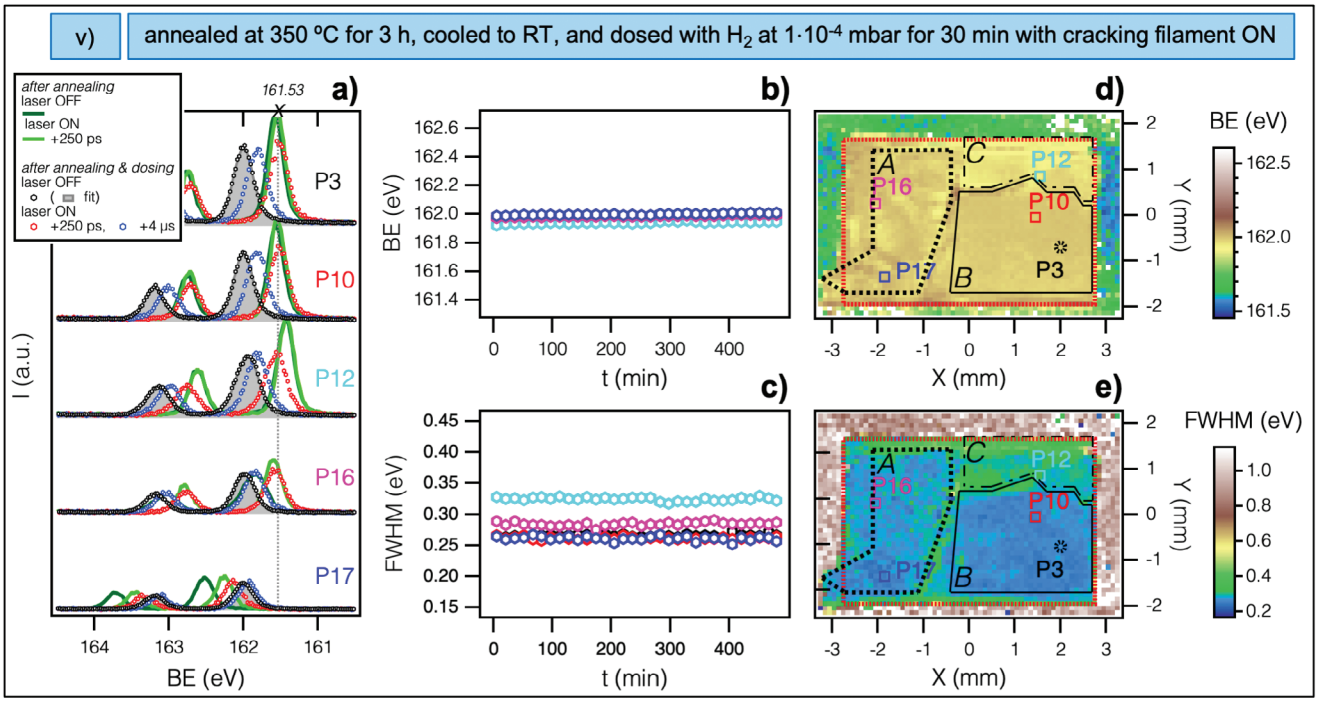

Figure 5. Treatment step (v): sample annealed (in ultra-high-vacuum (UHV)) at 350 °C for 3 h, then cooled to room temperature, and finally dosed with H_2 at 1×10^{-4} mbar for 30 min with cracking filament ON, thus effectively exposed to H. Same plots as described in the caption of Figure 2. As in Figure 4, panel (a) also shows X-ray photoelectron spectroscopy (XPS) spectra after the annealing pre-gas exposure (dark green/light green for S 2p laser-OFF/laser-ON at +250 ps pump-probe delay and ≈30 µJ cm^{-2} pump energy density).

intercalate deeper into the bulk in this part of the sample. The BEs still tend to drift to higher values over the initial several hours but the drifts are decidedly smaller (Figure 4b versus Figure 3b), thus—at equilibrium—the XY maps picture a situation very similar to that asymptotically reached after the previous annealing (Figure 4d,e versus Figure 3d,e, and Figure S2, Supporting Information). The effects of H_2 dosing are fully reversible with subsequent annealing, as it can be appraised by comparing the post-annealing spectra pre-H_2 exposure and pre-H exposure (green lines in Figure 4a versus Figure 5a).

To our knowledge, the only other study that has dealt with room temperature H_2 exposure of bulk MoS_2 is a work from Han et al.,[29] where a similar photon energy (and hence probing depth), but a lower H_2 pressure (1×10^{-6} Torr for up to 1 h) were used. According to density functional theory (DFT) calculations from these authors, H_2 physisorption does not lead to BE shifts, it is only when dissociated H_2 binds to exposed Mo atoms at S vacancies that the BE shifts to higher values. Accordingly, they reported no major BE shift upon H_2 exposure for a cleaved sample with S $2p_{3/2}$/VBM at ≈161.4/≈0.43 eV, but rather blurring of ARPES and growth of a new component at ≈1 eV higher BE than the main S 2p doublet. They also observed no BE shift for a C-containing air-exposed sample with S $2p_{3/2}$/VBM at ≈162.8/≈1.51 eV, nor for a C-containing cleaved sample with S $2p_{3/2}$/VBM at ≈162.3/≈0.35 eV, however they did observe a BE shift of ≈0.4 eV for a C-containing cleaved sample with S $2p_{3/2}$/VBM at ≈161.8/≈0.0 eV, which was explained with the latter surface being richer in S vacancy defects and dissociative H_2 chemisorption being dominant over H_2 physisorption. A VBM very close to the Fermi level is the norm rather than the exception for the macroscopically flat areas of our annealed C-free sample: the VBM is at ≈0.13/≈0.0 eV (in correspondence to a S $2p_{3/2}$ at ≈ 161.51/≈ 161.4 eV) for P3 and P12, respectively, and it increases by ≈0.24/≈0.13 eV upon H_2 exposure (Figures S3 and S4, Supporting Information). Yet, despite the S 2p peaks being narrower in our measurements, we do not detect the additional doublet at 0.75 eV lower BE that is noticeable in the measurements described in the aforementioned study[29] and attributed to S vacancies.

In the work from Cho et al.,[45] bulk MoS_2 has been studied under five orders of magnitude higher H_2 pressure (20 bar) and at milder temperature (80 °C), under which conditions H_2 is expected to dissociate and create S vacancies by formation of volatile H_2S. Based on their measurements, the fingerprints of such a scenario would be yet again very different, as they reported discrete flat valence bands near the Γ point—interpreted as signature of electron confinement within the top few layers—and no shift of the VBM, but a shift of the conduction band minimum (probed thanks to potassium doping) toward the Fermi level—interpreted as signature of a reduction in the interlayer spacing. These features are not apparent in our study.

The results of atomic hydrogen exposure are reported in Figure 5. H dosing produces peculiarly different results compared to H_2 dosing. The positions from the cleaved part of the sample, which had low BEs right after annealing, are now greatly shifted to higher BEs (and their laser-induced BE shifts are largely increased too), the position from the uncleaved part of the sample with intermediate BE right after annealing (P16) is now

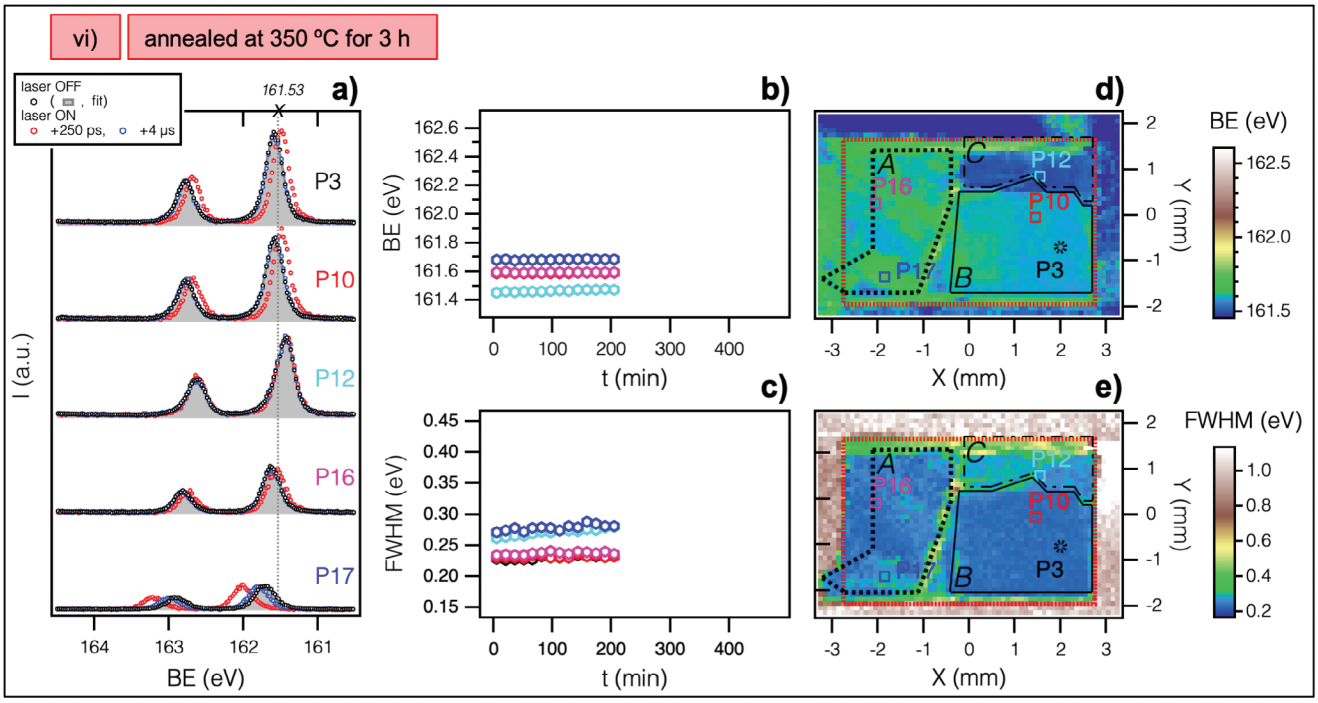

Figure 6. Treatment step (vi): sample annealed (in ultra-high-vacuum (UHV)) at 350 °C for 3 h. Same plots as described in the caption of Figure 2.

moderately shifted to higher BE, and the position from the uncleaved part of the sample with high BE right after annealing (P17) is now considerably shifted to lower BE, with the result that all sample positions end up having practically the same BE (Figure 5a). The laser-ON spectra remain peaked at the same values as before H exposure for P3, P10 and P16, the same value at which also the laser-ON spectrum of P12 aligns after H exposure. As for P17, its laser-ON spectrum is also altered by H exposure, but it remains out-of-trend with respect to the others, with the laser notably inducing a small BE shift toward the opposite direction. For the well-cleaved positions, a decrease in the peak height and an increase in the peak width are evident. All positions are now very stable over the usual several hours timespan preceding the acquisition of the XY maps (Figure 5 b,c). The latter confirm with striking clarity what already emerged from examining the few selected positions: the S $2p_{3/2}$ BE distribution across the sample surface has become much narrower and peaked at 162.0 eV (161.98 ± 0.025 eV more precisely, evaluated over 1890 sample positions); the FWHM distribution has also become narrower and peaked at the comparatively large value of 0.26 eV (Figure 5d,e and Figure S2, Supporting Information). As regions A and B now look indistinguishable in their surface energy levels, region C emerges as the slightly deviant one, with its BE/FWHM slightly lower/larger than the average. Moreover, changes in the valence band occur, which go beyond the so-far observed rigid BE shifts with respect to the core levels: there is a subtle transfer of intensity from above to below the valence band edge—highlighted for position P3 in Figure 7a (zoomed spectra in logarithmic scale). Additionally, the angular-resolved band structure reveals a broadening and a weakening of the energy bands and a clear increase of non-dispersive intensity between the relative maximum at the K point and the minimum of the topmost energy band. These effects are well visible for position P12 (Figure S4b–d, Supporting Information) as much as—if not more—than for position P3 (Figure 7 and Figure S3b–d, Supporting Information), while they are not noticeable for position P17 whose ARPES spectra are from the start weaker and more scattered (Figure S5b–d, Supporting Information).

Upon subsequent annealing, as illustrated in Figure 6a, the cleaved positions of regions C/B are completely/almost completely back to their low BEs and null/very small laser-induced BE shifts, although with a slight loss in intensity and a slight increase in FWHM. The uncleaved positions of region A—which had relatively high BEs until the annealing pre-H dosing—also undergo a shift to lower BEs, thus some degree of BE homogeneity across the sample is maintained (Figure 6a). Good stability over time is maintained as well (Figure 6b,c). The average FWHM, despite slightly smaller than after H-dosing, is still noticeably larger than the average FWHM of region B prior to H dosing (Figure 6e versus 5e versus 4e).

To further test the thermal stability of the hydrogen-treated sample, the latter was annealed again, first at the same temperature for yet another 3 h (preparation vii), and then for additional 2 h at 450° C (preparation viii). The results are in part presented in the Supporting Information. In brief: BEs are back to shifting toward higher values over time and, eventually, inhomogeneities in both BE and FWHM start to reappear, with a spatial distribution that recalls the one pre-H treatment (Figure S1f, Supporting Information). Moreover, the spectra develop a tail on the high BE side, which keeps increasing with progressive annealing and is most pronounced for the well-cleaved positions and, in particular, for the spot in region C (red solid lines labelled vi to pre-ix in Figures S3a, S4a, and S5a, Supporting Information). Finally it is to be noted that progressive annealing post-H exposure

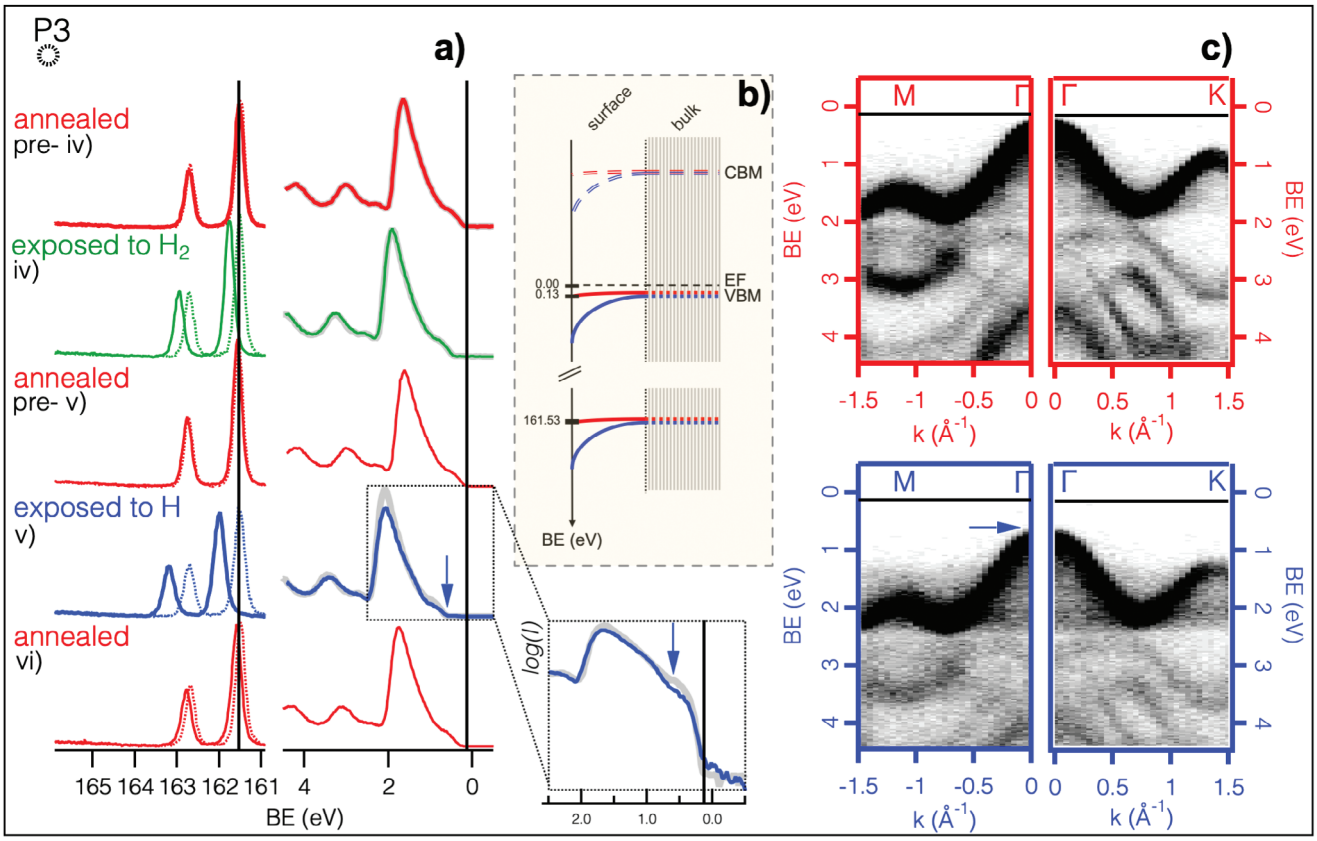

Figure 7. X-ray photoelectron spectroscopy (XPS) and angular-resolved photoelectron spectroscopy (ARPES) spectra for annealed and hydrogenated MoS_2 measured at position P3, representative of a relatively large homogenous, clean, and flat surface area. a) S 2p (left; solid lines for laser-OFF, dotted lines for laser-ON at +250 ps pump-probe delay and ≈30 μJ cm^{-2} pump energy density) and valence band (right; laser-OFF only) XPS spectra for annealed (red) versus H_2-dosed (green) versus H-dosed (blue) MoS_2. b) Energy level diagrams for surface and bulk, as derived from the laser-OFF and laser-ON spectra in (a), respectively, assuming a bandgap of 1.3 eV. c) Angular-resolved valence band spectra along the M-Γ and Γ-K directions in reciprocal space, of which the valence band spectra in a) are the angular integral. The black vertical lines in a) help to appreciate that the binding energy (BE) shifts are the same for the two energy regions. Overlapped to the valence band spectra for H_2-dosed and H-dosed MoS_2 in a) is the valence band spectrum for annealed MoS_2 rigidly shifted by +0.26 and +0.43 eV respectively (gray lines), showing that, while H_2 exposure only causes a BE shift, H exposure causes a BE shift plus a subtle redistribution of intensity above and below the valence band edge (blue arrow). The latter is best appreciable from the enlarged view with logarithmic intensity scale. The angular-resolved view in c) additionally shows that H exposure results in a growing non-dispersive background between the relative maximum at K and the minimum of the topmost band, concomitant with a weaking of the higher energy bands.

affects the laser-ON spectrum for P17, that gradually shifts toward lower BE until overlapping with the laser-OFF spectrum centered at the same value of ≈161.53 eV at which the laser-OFF and laser-ON spectra for P3 were centered after annealing pre-H exposure (red dotted lines labelled vi to pre-ix in Figure S5a, Supporting Information, see in particular pre-ix in Figure S5a versus pre-ix in Figure S3a). Although this result comes from a single sample position (P17 was the only one showing a laser-ON spectrum centered at a very different value) and therefore calls for more extensive verification, it possibly points to the important conclusion that, if exposure to atomic hydrogen makes the surface energy levels homogeneous, exposure to atomic hydrogen followed by prolonged annealing has a healing effect deeper into the bulk.

To verify how the hydrogen-treated sample would respond to ambient conditions, the sample was again dosed with H after a fresh annealing (preparation ix), then annealed at the same moderate conditions (preparation x), and finally brought in air for 1 h (plus the time for venting and pumping down again) (preparation xi). The second H treatment reproduces well the result of the first one, as it can be appreciated by the similarity of the corresponding XY maps (Figure S1g versus S1e, Supporting Information). Unfortunately, while in air, the sample was accidentally hit, which resulted in a visible flattening of the flaky border between region A and regions B/C (Figure S12c, Supporting Information), big versus small XY map of the sample relative height). Despite this unintentional modification of the sample, one can notice that the FWHM is to a good extent unchanged, both in its average value and in its spatial distribution across the sample surface; whereas the BE has increased everywhere, yet it has similar values within the central areas of the three regions, hence some level of homogeneity is retained (Figure S1h versus S1g, Supporting Information).

We will not present here the entire history of treatments for sample 2, for which we refer the reader to Figures S8–S11 in the Supporting Information. However, we mention the most notable

outcome. Namely, that exposure to atomic hydrogen at room temperature also resulted in a homogenization of the surface BE to the same S $2p_{3/2}$ peak value of ≈162.00 eV, in spite of the fact that dosing took place on a sample which was not freshly annealed and showed everywhere carbon contamination (notwithstanding previous cleaving and annealing to 350 °C).

To the best of our knowledge, no other experimental study has dealt with room temperature H exposure of bulk MoS_2. Reference[27], as mentioned above, has studied monolayer MoS_2 under cumulative room temperature H exposure (from H_2 at 2×10^{-5} mbar). They reported a gradual shift to lower BE, interpreted as gradual tuning of doping from n- to p-type, as H fills existing S vacancies at first, while eventually dynamically inducing and replacing new S vacancies at increasing doses, thereby resulting in an improvement of the ARPES quality. While the BE shift toward lower values for a S $2p_{3/2}$ spectrum originally peaked at 162.5 eV would be compatible with our findings for the sample positions of highest BEs, the ARPES quality is in our case either unaffected or worsen, in a way that may be rather suggestive of increased lattice disorder. At the same time, the homogenized surface potential suggests that local excesses and deficiencies of electrons on the MoS_2 surface may be compensated for through interaction with H.

A possible key to the interpretation of our results in this direction comes from Ferreira et al.,[21] who calculated the adsorption energies for H on monolayer MoS_2 and, at variance with the previously cited work from Cai et al.[25] (according to whom H eventually induces metallization), they located the transition level between the positive and negative charge states of adsorbed H close to the middle of the MoS_2 bandgap. Based on this, they concluded that hydrogen behaves in molybdenum disulfide as amphoteric impurity, i.e., it can trap majority carriers, and thus lead to charge compensation, in both n- and p-type doping conditions. This is no exotic behavior. In fact, the same occurs for example in silicon, where—citing Pearton et al.[46]—donor and acceptor dopants and a wide variety of impurities and defects are deactivated upon association with hydrogen. According to Van de Walle and Neugebauer,[47] there exists an universal alignment for the electronic transition level of hydrogen in semiconductors, insulators and even aqueous solutions, that allows to predict the electrical activity of H in any host material. For bulk MoS_2, considering a value of 5.47 eV for the ionization energy as found by Schlaf et al.,[48] such theoretical value of 4.5 eV for the H (+/−) transition level with respect to the vacuum level would fall 0.97 eV above the VBM, i.e., in the upper half of the bandgap. In our measurements, instead, the VBM after H exposure is found at roughly 0.56 eV BE, i.e., quite close to mid-gap.

In the literature, a few methods have been discussed to passivate defects in monolayer and few-layers MoS_2. Reversible passivation of charged defects by mere electrostatic screening was proposed for grounded MoS_2 in contact with an ionic liquid.[49] Temperature-aided reactions with thiol group containing molecules,[50,51] as well as O_2 non-dissociative chemisorption—also aided by annealing[52] or by laser irradiation[53]—were shown to passivate sulfur vacancies. Lu et al.[54] argued that hydrogen is not as effective of a passivant as it is in covalently bonded semiconductors such as silicon, because of the symmetry constraints implied by the multi-centered bonding in MoS_2. On the basis of DFT calculations, they established that proper passivation of a sulfur vacancy is only possible when the latter is bonded to a complex of three hydrogen atoms in the −1 charge state. Protonation of the three dangling bonds at each sulfur vacancy site was adduced as a possible explanation for why treatment with the organic superacid bis(trifluoromethane) sulfonamide (TFSI) achieves close-to-ideal photoluminescence quantum yield in monolayer MoS_2, unlike treatment with the analogue compound N-phenyl-bis(trifluoromethane)sulfonimide (Ph-TFSI), where hydrogen is replaced by a phenyl group.[55] However, given that the energetics of such process appears unfavorable, Amani et al.[55] suggested that hydrogen may rather facilitate a restructuring of the surface to reduce sulfur vacancies through rearrangement of sulfur adatoms. We speculate that our findings could be indicative of a similar scenario. Although parallel S and Mo XPS spectra are not available from our measurements, such hypothesis possibly finds further support in an old XPS study[56] according to which—starting from a S $2p_{3/2}$ BE of 162.4 eV and a S/Mo atomic ratio of 2.2 for single crystal MoS_2 cleaved in air—Ar-ion bombardment after moderate annealing resulted in a progressive lowering of the S $2p_{3/2}$ BE and of the S/Mo atomic ratio: notably, a S $2p_{3/2}$ BE of 162.0 eV was found in correspondence with a stoichiometric S to Mo ratio of 2.0.

3. Conclusions

We presented a XPS study of single-crystalline bulk MoS_2 commercially produced by chemical vapor transport. X-ray pulses from a synchrotron were used to generate a surface-sensitive photoelectron probe, and visible light pulses from a synchronized ultrafast laser were used to induce above-bandgap excitation in the sample. Combining laser-OFF and laser-ON measurements allowed us to follow the S 2p and valence band binding energies at the surface and in the bulk, as the sample was subject to cleaning procedures commonly used for the preparation of crystals under UHV conditions.

We made the following observations.

Bulk binding energies are for the most part homogenous across the sample, compatible with p-type doping, and not affected by thermal annealing nor exposure to molecular or atomic hydrogen. Surface binding energies, on the other hand, may largely differ at different sample positions after in-vacuum cleaving, partly owing to different amounts of contaminants, partly owning to—potentially—a variety of different reasons. The surface band bending is correspondingly of varying amplitude, but always null or downward-oriented, indicative of the formation of an electron accumulation layer within the near-surface region. Surface binding energies can undergo sizable shifts over a timespan of several hours since in-vacuum cleaving, likely due to an interaction with residual gases in the measurement chamber. These shifts are also of varying amplitude, but always null or toward higher surface binding energies, indicative of occurred charge transfer from the gases toward the MoS_2 surface. Even after such shifts have stabilized, huge variations in the surface potential persist across the surface.

Upon annealing to 350 °C, carbon contamination—at times still present despite the cleavage—is typically removed from the surface. At flat, well-cleaved regions, the surface binding energies are variously lowered, and the surface band bending vanishes.

Over time, only for some of those positions the surface binding energies shift toward higher values, so—eventually—the surface binding energy distribution is even broader than after cleaving.

Dosing of molecular hydrogen at room temperature on a freshly annealed sample variously increases the surface binding energies of the flat, well-cleaved regions, and suppresses all surface binding energy shifts over time, yet the surface binding energies continue to differ from position to position.

Dosing of atomic hydrogen at room temperature on a freshly annealed sample, instead, not only suppresses surface binding energy shifts over time, but levels out all surface S $2p_{3/2}$ binding energies to a common value of ≈162.0 eV, which corresponds to a Fermi level roughly in the middle of the indirect bandgap. The hydrogenated sample shows broadened core-levels and a redistribution of intensity across the topmost valence band. Upon successive annealing, discrete homogeneity is preserved, but at lower surface binding energies and small to no band bending.

We interpret the remarkable effectiveness of atomic hydrogen in lifting any surface inhomogeneity as stemming from its ability to either donate or accept electrons, thereby balancing charge defects and impurities likely present on the cleaved surface.

4. Experimental Section

The samples were purchased from 2D Semiconductors USA and kept in their sealed boxes up until the measurement campaign.

They were mechanically cleaved using scotch tape, first in air shortly before introduction in the vacuum system, then again in a preparation chamber held at a pressure below 5×10^{-9} mbar just before the start of the investigation in the analysis chamber held at a pressure below 1×10^{-9} mbar.

For each new preparation, the sample was transferred from the measurement chamber to the preparation chamber, then back to the measurement chamber. Such transfers could result in a slight offset in sample positioning, which is however estimated to be well below the size of the probing X-ray beam.

During radiative thermal annealing, the temperature was monitored by a thermocouple located at the manipulator and previously calibrated against a PT100 sensor located at the sample position.

The stated gas dosing pressure of 1×10^{-4} mbar was as read by a PKR 261 vacuum gauge with default calibration.

The measurements took place at the LowDosePES end-station[30] of the PM4 beamline of the BESSY II synchrotron. The beamline was operated in pseudo-single-bunch mode during regular hybrid-bunch operation of the synchrotron, i.e., with a MHz chopper wheel letting toward the end-station only the radiation produced by one 4 mA pulse every 800 ns.

Photons of 215 and 55 eV energy were used to excite S 2p XPS and valence band spectra, respectively, in order to obtain optimal surface sensitivity and good energy resolution. Considering both contributions from the photon source (≈92 and ≈12 meV at 214 and 55 eV photon energy, respectively) and from the angular-resolved time-of-flight (ArTOF) electron analyzer (≈49 meV at 50 eV kinetic energy), the total energy resolution was estimated as 104 and 50 meV for S 2p and valence band, respectively. In the chosen acquisition mode, the ArTOF had an angular resolution of ≈0.1° and an angular acceptance of ≈35°. The binding energy scale was calibrated using either the Au $4f_{7/2}$ peak or the Fermi edge of a polycrystalline Au sample, fixed at 84.00 eV and 0.00 eV respectively.

Each S 2p XPS spectrum was fitted to a pair of Voigt peaks on a cubic background, with fixed Lorentzian width of 90 meV, energy separation of 1.197 eV and intensity ratio of 0.5, and variable Gaussian width, energy position, intensity, and background parameters. The values of 90 meV for the Lorentzian width and of 1.197 eV for the xenergy separation were determined as the average of the results of parameters-free fits for the timeseries at positions P1, P2, P3, P4, and P6 of sample 1 after treatment step (i).

The S 2p signal from crystalline MoS_2 has a high throughput at the described settings. Nevertheless, each of the presented XY maps contains few thousand spectra. Hence, to minimize the acquisition time, an on-the-flight acquisition mode was developed, whereby a single ArTOF instance is launched per map (versus executing a call to the ArTOF acquisition software after each movement of the manipulator), and a post-measurement script sorts the "motion-free" data into a 4D map of spectrum versus manipulator X and Y coordinates. With an acquisition time of 15 s per spectrum and an average manipulator motion time of less than a couple of seconds per step, the acquisition of each map for sample 1 overall required about 13.5 h (≈2900 points, ≈16.7 s point^{-1} on average).

The C 1s XPS signal was also regularly monitored (using 500 eV photons), as we became aware that, while in most cases annealing gets rid of carbon—like for the case of sample 1 discussed in the main text—in few cases it may not be so—like for the case of sample 2 discussed in Supporting Information.

O 1s and Mo 3d XPS spectra were measured only occasionally (using 620 and 326 eV photons, respectively). In the numerous investigations, oxygen was found in negligible amounts. As for molybdenum, it was found unfeasible to systematically monitor it at each preparation step and multiple positions, as—at this setup—the collection time for a Mo 3d spectrum with good statistics is significantly longer than the collection time for a S 2p spectrum of corresponding quality. However, the existing data allow to say that the variation in Mo 3d peak positions among different sample spots mimics the variation in the corresponding S 2p peak positions, i.e., the spectra are rigidly shifted, as already observed from the comparison between S 2p and valence band spectra. Furthermore, also for the Mo 3d spectra no extra peaks are detectable other than the main Mo^{4+}-related doublet.

Assessment of the direction and amount of surface band bending was possible thanks to a synchronized laser operated at 515 nm wavelength, ≈350 fs pulse length and 208.333 kHz repetition rate (corresponding to 1/6 of the X-rays revolution frequency). The laser was focused to a spot of ≈210 µm diameter, roughly double the size of the X-ray spot. Spatial overlap between laser and X-rays was achieved with the help of a fluorescent screen and a microscope camera. Temporal overlap was established using the ArTOF to detect the arrival times of the two photon beams and a phase shifter to adjust at will the delay of the laser relative to the X-rays.

S 2p spectra were measured at a pump-probe delay of +250 ps as a function of laser power for a MoS_2 sample introduced in the measurement chamber without prior cleaving (neither in UHV nor in air). It has been found in preparatory work that has set the stage for the measurements presented here that in these conditions (of strong contamination from—presumably[57]—hydrocarbons) one can reach the largest surface band bending, hence in this work we have chosen the laser power slightly above the value for which laser-induced BE shifts are saturated at this sample and judged such settings to be suitable to probe flat band conditions for the investigated cleaved samples. Laser power scans collected for each preparation step, at selected positions, at the end of the XY maps, indeed confirmed the suitability of ≈7 mW to saturate the laser-induced BE shifts, corresponding to an energy density per pulse of ≈30 µJ cm^{-2}. Figure S6 (Supporting Information) shows such laser power scans for selected sample preparations and positions. For the same selected sample preparations and positions, Figure S7 (Supporting Information) shows pump-probe delay scans at ≈30 µJ cm^{-2}, covering the range between −400 and +400 ps at steps of 25 ps and the range between +400 ps and +400 ns in 10 logarithmic steps. The choice of a too high laser fluence may result in small residual laser-induced BE shifts persisting for up to several hours after the laser has been turned off, eventually even at neighboring sample positions. Knowing that from previous campaigns, in this work we acquired laser-OFF spectra both before and after the laser-ON spectra, and thus systematically verified that, under the conditions of this experiment, the laser is not inducing any long-leaved—let alone permanent—effect.

Supporting Information

Supporting Information is available from the Wiley Online Library or from the author.

Acknowledgements

The present work was conducted at the LowDosePES end-station, whose funding from the Uppsala Berlin joint Laboratory on Next Generation Electron Spectroscopy is acknowledged. The authors also thank the Helmholtz-Zentrum Berlin für Materialien und Energie for the allocation of synchrotron radiation beamtime.

Open access funding enabled and organized by Projekt DEAL.

Conflict of Interest

The authors declare no conflict of interest.

Data Availability Statement

The data that support the findings of this study are available from the corresponding author upon reasonable request.

Keywords

molybdenum disulphide, sample inhomogeneity, hydrogen adsorption, surface passivation, transition metal dichalcogenides

Received: May 11, 2023
Revised: June 12, 2023
Published online: August 31, 2023

[1] I. Song, C. Park, H. C. Choi, *RSC Adv.* **2015**, *5*, 7495.
[2] C. N. R. Rao, K. Gopalakrishnan, U. Maitra, *ACS Appl. Mater. Interfaces* **2015**, *7*, 7809.
[3] S. K. Mahatha, K. S. R. Menon, *J. Phys.: Condens. Matter* **2012**, *24*, 305502.
[4] S. Mattila, J. A. Leiro, M. Heinonen, T. Laiho, *Surf. Sci.* **2006**, *600*, 5168.
[5] S. McDonnell, R. Addou, C. Buie, R. M. Wallace, C. L. Hinkle, *ACS Nano* **2014**, *8*, 2880.
[6] M. Donarelli, F. Bisti, F. Perrozzi, L. Ottaviano, *Chem. Phys. Lett.* **2013**, *588*, 198.
[7] X. Zhang, S. Wang, C.-K. Lee, C.-M. Cheng, J.-C. Lan, X. Li, J. Qiao, X. Tao, *Phys. Chem. Chem. Phys.* **2020**, *22*, 21776.
[8] J. R. Lince, T. B. Stewart, M. M. Hills, P. D. Fleischauer, J. A. Yarmoff, A. Taleb-Ibrahimi, *Surf. Sci.* **1989**, *223*, 65.
[9] C. A. Papageorgopoulos, W. Jaegermann, *Surf. Sci.* **1995**, *338*, 83.
[10] E. Lee, Y. S. Yoon, D.-J. Kim, *ACS Sens.* **2018**, *3*, 2045.
[11] H. Zhang, R. Lv, *J. Mater.* **2018**, *4*, 95.
[12] Q. Yue, Z. Shao, S. Chang, J. Li, *Nanoscale Res. Lett.* **2013**, *8*, 425.
[13] H. Li, M. Huang, G. Cao, *Phys. Chem. Chem. Phys.* **2016**, *18*, 15110.
[14] H. Qiu, L. Pan, Z. Yao, J. Li, Y. Shi, X. Wang, *Appl. Phys. Lett.* **2012**, *100*, 123104.
[15] S. Tongay, J. Zhou, C. Ataca, J. Liu, J. S. Kang, T. Matthews, L. You, J. Li, J. C. Grossman, J. Wu, *Nano Lett.* **2013**, *13*, 2831.
[16] R. V. Mom, J. N. Louwen, J. W. M. Frenken, I. M. N. Groot, *Nat. Commun.* **2019**, *10*, 2546.
[17] Q. Ding, B. Song, P. Xu, S. Jin, *Chem* **2016**, *1*, 699.
[18] M. Sun, A. E. Nelson, J. Adjaye, *Catal. Today* **2005**, *105*, 36.
[19] B. H. Kim, M. Park, M. Lee, S. J. Baek, H. Y. Jeong, M. Choi, S. J. Chang, W. G. Hong, T. K. Kim, H. R. Moon, Y. W. Park, N. Park, Y. Jun, *RSC Adv.* **2013**, *3*, 18424.
[20] J. Cao, J. Zhou, Y. Zhang, X. Liu, P. Si, *Microelectron. Eng.* **2018**, *190*, 63.
[21] F. Ferreira, A. Carvalho, Í. J. M. Moura, J. Coutinho, R. M. Ribeiro, *J. Phys.: Condens Matter* **2018**, *30*, 035003.
[22] E. W. Keong Koh, C. H. Chiu, Y. K. Lim, Y.-W. Zhang, H. Pan, *Int. J. Hydrogen Energy* **2012**, *37*, 14323.
[23] Z. Zhu, H. Peelaers, C. G. Van de Walle, *Phys. Rev. B* **2016**, *94*, 085426.
[24] I. N. Yakovkin, N. V. Petrova, *Chem. Phys.* **2014**, *434*, 20.
[25] Y. Cai, Z. Bai, H. Pan, Y. P. Feng, B. I. Yakobson, Y.-W. Zhang, *Nanoscale* **2014**, *6*, 1691.
[26] Y. Xu, Y. Li, X. Chen, C. Zhang, R. Zhang, P. Lu, *AIP Adv.* **2016**, *6*, 075001.
[27] D. Pierucci, H. Henck, Z. B. Aziza, C. H. Naylor, A. Balan, J. E. Rault, M. G. Silly, Y. J. Dappe, F. Betran, P. Le Fèvre, F. Sirotti, A. T. C. Johnson, A. Ouerghi, *ACS Nano* **2017**, *11*, 1755.
[28] S. W. Han, W. S. Yun, J. D. Lee, Y. H. Hwang, J. Baik, H. J. Shin, W. G. Lee, Y. S. Park, K. S. Kim, *Phys. Rev. B* **2015**, *92*, 241303.
[29] S. W. Han, G.-B. Cha, Y. Park, S. C. Hong, *Sci. Rep.* **2017**, *7*, 7152.
[30] E. Giangrisostomi, R. Ovsyannikov, F. Sorgenfrei, T. Zhaang, A. Lindblad, Y. Sassa, U. B. Cappel, T. Leitner, R. Mitzner, S. Svensson, N. Mårtensson, A. Föhlisch, *J. Electron Spectrosc. Relat. Phenom.* **2018**, *224*, 68.
[31] K. K. Kam, B. A. Parkinson, *J. Phys. Chem.* **1982**, *86*, 463.
[32] C.-P. Lu, G. Li, J. Mao, L.-M. Wang, E. Y. B. Andrei, and Gating Effects in MoS_2, *Nano Lett.* **2014**, *14*, 4628.
[33] Z. Zhang, J. T. Yates, *Chem. Rev.* **2012**, *112*, 5520.
[34] When not differently specified, it is implied that the measurements were taken with laser OFF.
[35] Those regions will be henceforth referred to as uncleaved, meaning that they did not undergo proper UHV cleaving, however they have been cleaved previously in air. Correspondingly, well-cleaved positions will be simply referred to as cleaved.
[36] R. Kadowaki, N. Sano, T. Abukawa, *e-J. Surf. Sci. Nanotechnol.* **2017**, *15*, 115.
[37] R. Addou, S. McDonnell, D. Barrera, Z. Guo, A. Azcatl, J. Wang, H. Zhu, C. L. Hinkle, M. Quevedo-Lopez, H. N. Alshareef, L. Colombo, J. W. P. Hsu, R. M. Wallace, *ACS Nano* **2015**, *9*, 9124.
[38] J. H. Kim, J. Lee, J. H. Kim, C. C. Hwang, C. Lee, J. Y. Park, *Appl. Phys. Lett.* **2015**, *106*, 251606.
[39] S. Y. Lee, U. J. Kim, J. Chung, H. Nam, H. Y. Jeong, G. H. Han, H. Kim, H. M. Oh, H. Lee, H. Kim, Y.-G. Roh, J. Kim, S. W. Hwang, Y. Park, Y. H. Lee, *ACS Nano* **2016**, *10*, 6100.
[40] W. Bao, X. Cai, D. Kim, K. Sridhara, M. S. Fuhrer, *Appl. Phys. Lett.* **2013**, *102*, 042104.
[41] M. H. Naik, M. Jain, *Phys. Rev. Mater.* **2018**, *2*, 084002.
[42] S. Park, T. Schultz, X. Xu, B. Wegner, A. Aljarb, A. Han, L.-J. Li, V. C. Tung, P. Amsalem, N. Koch, *Commun. Phys.* **2019**, *2*, 109.
[43] The valence band maximum is estimated as the very onset of the energy distribution curve at the Γ point, which is identifiable with an accuracy better than 0.25 eV due to the leading edge of such curve being very steep.
[44] The experimental uncertainty on the XPS signal intensities is dictated by the possible long-term flux instability of the X-ray beamline and the possible irreproducibility of the sample positioning with respect to the manipulator coordinates upon transfer of the sample from the measurement chamber to the preparation chamber and back to the measurement chamber.

[45] S. Cho, B. S. Kim, B. Kim, W. Kyung, J. Seo, M. Park, J. W. Jeon, K. Tanaka, J. D. Denlinger, C. Kim, D. Odkhuu, B. H. Kim, S. R. Park, *Phys. Chem. Chem. Phys.* **2018**, *20*, 23007.
[46] S. J. Pearton, J. W. Corbett, M. Stavola, *Hydrogen in Crystalline Semiconductors*, Vol. *16*, Springer, Berlin Heidelberg **1992**.
[47] C. G. Van de Walle, J. Neugebauer, *Nature* **2003**, *423*, 626.
[48] R. Schlaf, O. Lang, C. Pettenkofer, W. Jaegermann, *J. Appl. Phys.* **1999**, *85*, 2732.
[49] T. L. Atallah, J. Wang, M. Bosch, D. Seo, R. A. Burke, O. Moneer, J. Zhu, M. Theibault, L. E. Brus, J. Hone, X.-Y Zhu, *J. Phys. Chem. Lett.* **2017**, *8*, 2148.
[50] Z. Yu, Y. Pan, Y. Shen, Z. Wang, Z.-Y. Ong, T. Xu, R. Xin, L. Pan, B. Wang, L. Sun, J. Wang, Y. W. Zhang, Y. Shi, X. Wang, *Nat. Commun.* **2014**, *5*, 5290.
[51] D. M. Sim, M. Kim, S. Yim, M.-J. Choi, J. Choi, S. Yoo, Y. S. Jung, *ACS Nano* **2015**, *9*, 12115.
[52] P. K. Gogoi, Z. Hu, Q. Wang, A. Carvalho, D. Schmidt, X. Yin, Y.-H. Chang, K.-J. Li, C. H. Sow, A. H. C. Neto, M. B. H. Breese, A. Rusydi, A. T. S. Wee, *Phys. Rev. Lett.* **2017**, *119*, 077402
[53] R. Rao, V. Carozo, Y. Wang, A. E. Islam, N. Perea-Lopez, K. Fujisawa, V. H. Crespi, M. Terrones, B. Maruyama, *2D Mater.* **2019**, *6*, 045031.
[54] H. Lu, A. Kummel, J. Robertson, *APL Mater.* **2018**, *6*, 066104.
[55] M. Amani, D. H. Lien, D. Kiriya, J. Xiao, A. Azcatl, J. Noh, S. R. Madhvapathy, R. Addou, S. KC, M. Dubey, K. Cho, R. M. Wallace, S.-C. Lee, J.-H. He, W. Ager III, J., X. Zhang, E. Yablonovitch, A. Javey, *Science* **2015**, *350*, 1065.
[56] N. S. McIntyre, P. A. Spevack, G. Beamson, D. Briggs, *Surf. Sci.* **1990**, *237*, L390.
[57] A. Kozbial, X. Gong, H. Liu, L. Li, *Langmuir* **2015**, *31*, 8429.